International Journal of Fatigue 176 (2023) 107910

Contents lists available at ScienceDirect

International Journal of Fatigue

journal homepage: www.elsevier.com/locate/ijfatigue

Low cycle fatigue behaviour of wire arc additively manufactured ER70S-6 steel

Liang Zong [a,b], Wanquan Fang [a], Cheng Huang [c,*], Zhongxing Wang [a,b], Leroy Gardner [c]

[a] School of Civil Engineering, Tianjin University, Tianjin 300072, China
[b] Key Laboratory of Coast Civil Structure Safety (Tianjin University), Ministry of Education, Tianjin 300072, China
[c] Department of Civil and Environmental Engineering, Imperial College London, London SW7 2AZ, UK

ARTICLE INFO

Keywords:
Low cycle fatigue
Metal 3D printing
Non-Masing behaviour
Strain-life relationship
Wire arc additive manufacturing (WAAM)

ABSTRACT

Wire arc additive manufacturing (WAAM) is a method of 3D printing that is well suited to the cost-sensitive construction industry. Fundamental test data on the mechanical properties of WAAM materials, especially under cyclic loading, are however lacking. To bridge this gap, an experimental study into the low cycle fatigue (LCF) behaviour of WAAM ER70S-6 steel has been conducted and is presented herein. Following quasi-static mechanical and geometric characterisation, a series of as-built and machined coupons was tested in different directions relative to the print layer orientation ($\theta = 0°$, 45° and 90°) under constant amplitude LCF loading, covering a range of strain amplitudes from ±0.2% to ±2.0%. Fractographic analysis of the tested coupons was also performed to assess their failure mechanisms. On the basis of the experimental results, strain-life relationships and cyclic stress-strain curves were derived. The geometric undulations of the as-built coupons resulted in a weakening in the LCF properties, and the weakening effect increased with the loading angle θ and strain amplitude. The cyclic hardening/softening response of the WAAM material varied with the imposed strain amplitudes, while significant non-Masing behaviour was observed.

1. Introduction

The structural engineering and construction industries are moving towards greater automation through the adoption of digitally-enabled technologies, such as 3D printing [1,2], which is already impacting the aerospace [3], automotive [4] and medical [5] industries. Wire arc additive manufacturing (WAAM) is a metal 3D printing technique that uses metal wire as the feedstock material and a welding arc as the fusion source to build parts in a layer-upon-layer fashion. WAAM enables large-scale, complex-shaped parts to be produced with reasonable build times and costs, making it well-suited to the construction industry [6,7].

Applications of WAAM in construction have only emerged in recent years and include examples such as complex connection nodes [8], lightweight diagrid columns [9], a steel bridge in Darmstadt [10] and the stainless steel MX3D bridge in Amsterdam [11,12], with the latter being a landmark demonstrator of WAAM for structural uses. A series of experimental studies on WAAM structural elements have also been performed, aimed at investigating their behaviour at the material [13–15], cross-sectional [16–18], member [19,20], connection [21–23] and structural system [12,24] levels.

Knowledge concerning the fatigue properties of WAAM materials is currently rather limited, though a number of studies have recently been conducted. It has been shown that WAAM stainless steels exhibited inferior resistance to fatigue crack initiation [25] but superior resistance to fatigue crack propagation [26] relative to conventional structural steels. The surface undulations inherent to the WAAM process have been shown to have a detrimental effect on both the fatigue crack initiation and propagation behaviour of WAAM materials [27–29]. Several experimental studies [30–32] into the fatigue crack growth behaviour of machined WAAM ER70S-6 steel plates have recently been performed and revealed comparable crack propagation rates compared to S355 structural steel. More recently, Huang et al. [33] conducted a comprehensive experimental and numerical study into the fatigue behaviour of WAAM steel plates in both the as-built and machined conditions, showing that the surface undulations resulted in a reduction of about 35% in the fatigue endurance limit for the as-built material relative to the machined material, and a reduction of about 60% in the fatigue life for the same cyclic load level. Overall, previous fatigue studies on WAAM materials have focused primarily on high cycle fatigue behaviour. Studies into the low cycle fatigue properties of WAAM steel are

* Corresponding author.
E-mail address: cheng.huang118@imperial.ac.uk (C. Huang).

https://doi.org/10.1016/j.ijfatigue.2023.107910
Received 24 May 2023; Received in revised form 28 July 2023; Accepted 23 August 2023
Available online 24 August 2023

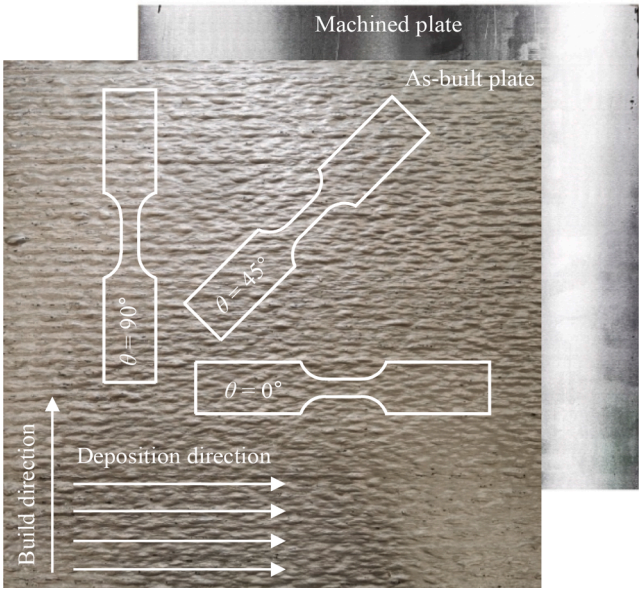

Fig. 1. Illustration of coupon extraction and deposition strategy for WAAM plates.

Table 1
Process parameters used for WAAM plates.

Process parameters	Details
Travel speed (mm/s)	8
Wire feed rate (m/min)	4
Welding voltage (V)	24.8
Welding current (A)	130
Gas flow rate (L/min)	16
Welding mode	Pulsed welding
Shielding gas	82% Ar + 18% CO_2
Dwell time (s)	30

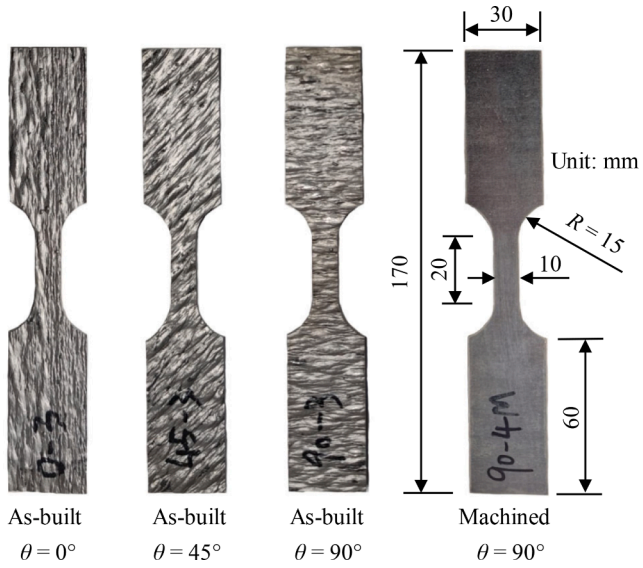

Fig. 2. Typical as-built and machined LCF coupons and nominal dimensions of all coupons.

scarce; this is therefore the focus of the current paper.

In the present study, low cycle fatigue tests on 31 as-built and machined WAAM coupons are described; the microscopic fracture characteristics of the tested coupons are also presented. Key mechanical properties obtained from previous tensile coupon tests [13] on the examined WAAM material are first summarised. The manufacture, geometric measurement and low cycle fatigue tests of the WAAM coupons are then described, followed by a discussion of the test results. Finally, the failure mechanisms of the tested WAAM coupons are investigated through fractography.

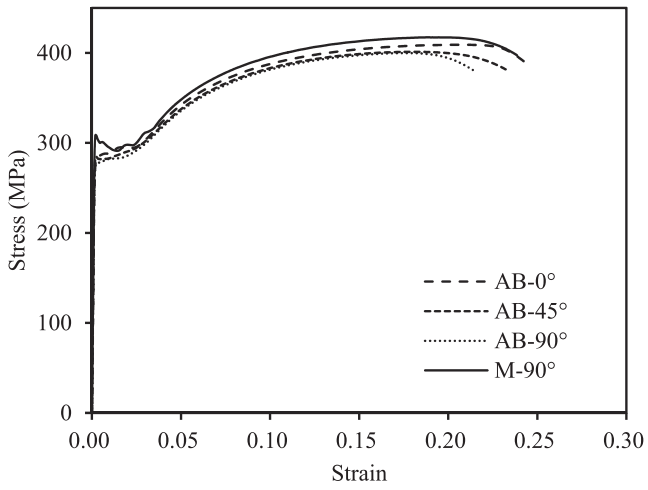

Fig. 3. Typical engineering stress-strain curves of examined WAAM material (AB = as-built; M = machined).

Table 2
Average measured mechanical properties of WAAM coupons [13].

Surface finish	θ (°)	E (MPa)	f_y (MPa)	f_u (MPa)
As-built	0°	203,800	290	406
	45°	201,900	289	409
	90°	199,000	281	403
Machined	90°	204,500	305	416

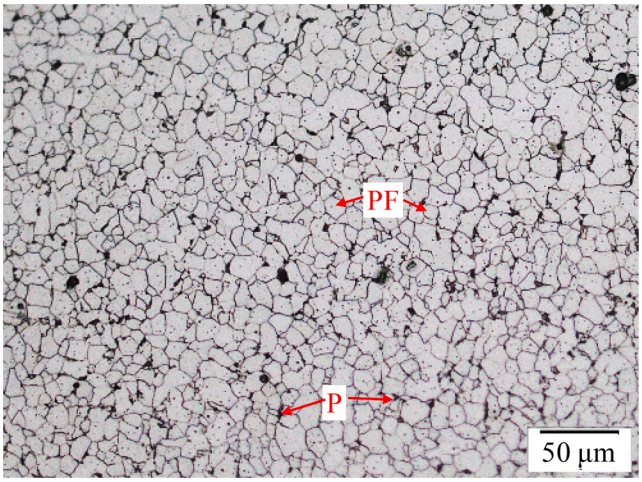

Fig. 4. Typical optical micrograph of examined WAAM material [13].

2. Experimental programme

2.1. Test specimens

Flat plates of 8 mm nominal thickness were cut from oval tubes (with flat sides), printed by MX3D [34] using ER70S-6 (EN ISO 14341-A G 42 3M21 3Si1) steel wire of 1.2 mm diameter. The chemical composition and mechanical properties of the as-welded feedstock material have

Fig. 5. Laser scanning of a typical fatigue coupon.

been reported in [13]. The WAAM plates were wire arc additively manufactured using the parallel deposition strategy [13,35], with a constant deposition direction throughout printing – see Fig. 1. A summary of the adopted WAAM process parameters is provided in Table 1. Fatigue coupons were extracted from the as-built WAAM plates at 0°, 45° and 90° relative to the print layer direction (i.e. $\theta = 0°$, 45° and 90°, see Fig. 1), to investigate any anisotropy in the low cycle fatigue (LCF) properties. A series of $\theta = 90°$ coupons, extracted from machined (with the surface undulations removed using a slitting saw) WAAM plates, was also examined, to isolate the influence of the geometric irregularities on the LCF properties. Note that residual stresses induced in the WAAM material during the production process would have reduced to some extent after specimen extraction and surface machining. Typical $\theta = 0°$, 45° and 90° as-built coupons and $\theta = 90°$ machined coupons are shown in Fig. 2, where the coupon dimensions, determined in accordance with BS ISO 12106 [36], are also presented. The coupon labelling system begins with the type of specimen (AB = as-built; M = machined), followed by the orientation relative to the print layer direction in degrees and a number to identity each coupon.

2.2. Mechanical properties and microstructure

Quasi-static mechanical and microstructural testing of the studied WAAM steel has been described by Huang et al. [13]. Typical measured stress-strain curves are presented in Fig. 3, and the key mechanical properties, including the Young's modulus E, yield strength f_y and ultimate tensile strength f_u, are summarised in Table 2. As expected, the as-built material exhibited inferior mechanical properties compared to the machined material due to the detrimental influence of the surface undulations. A typical optical micrograph of the WAAM steel is shown in Fig. 4, where a ferritic-pearlitic microstructure, featuring predominantly equiaxed grains (with an average grain size of 12.1 μm), can be observed. This microstructure is typical of conventional non-alloyed structural mild steels. The obtained mechanical and microstructural properties provided a basis for the design of the LCF tests and the subsequent fatigue analysis.

2.3. Geometric properties

Before cyclic testing, geometric measurements of the WAAM coupons were performed using 3D laser scanning, as shown in Fig. 5. The scan models were processed in Rhino 3D, whereby a set of operations was conducted for geometric analysis, including contouring the models along the longitudinal direction (i.e. the global x axis – see Fig. 6) and extracting grid points from the contours. The contours were used to calculate the cross-sectional areas along the parallel length of the coupons, while the grid points were used to determine the wall thickness and other cross-sectional dimensions. To achieve both computational efficiency and accuracy, a contour spacing of 0.1 mm was taken along both the x and y axes (i.e. $dx = dy = 0.1$ mm), as determined through a sensitivity study [13]. The obtained geometric properties of the WAAM coupons are summarised in Table 3, where A, A_{min} and A_{sd}, and t, t_{min} and t_{sd} are the average, minimum and standard deviation values of the cross-sectional area and thickness, respectively, e_y and e_z are the average centroid eccentricities in the y and z directions, respectively. The $\theta = 90°$ coupons are shown to exhibit a higher level of geometric variability than the $\theta = 0°$ and $\theta = 45°$ coupons, as reflected in the higher values of A_{sd}/A and t_{sd}/t.

Roughness is quantified by the deviations in the direction of the normal vector of a real surface from its ideal form, and was determined for the WAAM material following the procedure recommended in [28,33], which involved first filtering of the waviness and thickness deviation along the coupon length. Values of three typical surface roughness parameters have been determined for each of the test specimens and are summarised in Table 3, including the maximum roughness R_z, mean arithmetic height R_a and mean square height R_q, as given by Eqs. (1)–(3), respectively:

$$R_z = z_{max}(x,y) - z_{min}(x,y) \tag{1}$$

$$R_a = \frac{1}{S}\iint_S |z(x,y)|dxdy \tag{2}$$

$$R_q = \sqrt{\frac{1}{S}\iint_S z^2(x,y)dxdy} \tag{3}$$

where $z(x,y)$ is the coordinates of the grid points along the thickness direction and S denotes the surface area.

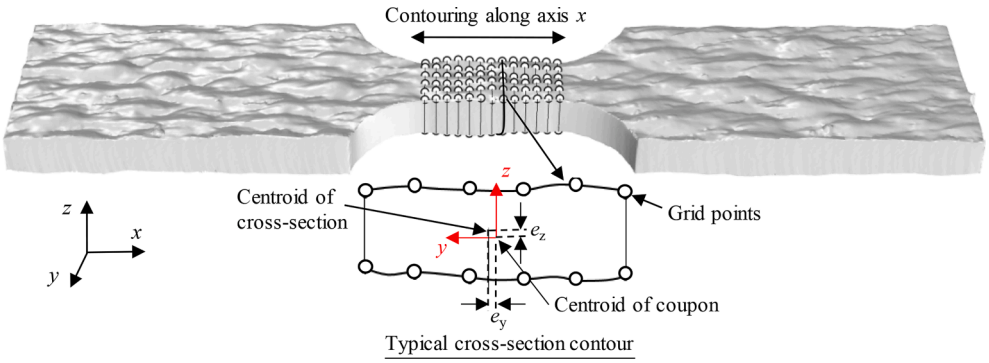

Fig. 6. Typical coupon geometry processed in Rhino 3D [13].

Table 3
Average geometric properties of WAAM coupons.

Types	A (mm^2)	$\frac{A_{min}}{A}$	$\frac{A_{sd}}{A}$	t (mm)	$\frac{t_{min}}{t}$	$\frac{t_{sd}}{t}$	$\frac{\lvert e_y \rvert}{t}$	$\frac{\lvert e_z \rvert}{t}$	R_z (mm)	R_a (mm)	R_q (mm)
AB-0-1	78.66	0.96	0.027	7.69	0.57	0.059	0.009	0.015	1.619	0.250	0.306
AB-0-2	81.17	0.97	0.023	7.92	0.60	0.063	0.014	0.015	1.759	0.283	0.346
AB-0-3	82.61	0.97	0.017	7.93	0.67	0.062	0.013	0.004	1.080	0.215	0.336
AB-0-4	81.70	0.95	0.035	7.87	0.87	0.051	0.006	0.016	1.268	0.202	0.268
AB-0-5	83.91	0.97	0.014	8.06	0.04	0.062	0.036	0.020	1.067	0.218	0.283
AB-0-6	84.91	0.96	0.015	8.10	0.82	0.037	0.005	0.011	1.263	0.183	0.229
AB-0-8	85.45	0.96	0.021	8.19	0.80	0.045	0.008	0.022	1.211	0.198	0.240
AB-0-9	78.36	0.97	0.015	7.62	0.79	0.045	0.006	0.007	1.576	0.228	0.444
AB-0-10	76.32	0.97	0.017	7.37	0.45	0.059	0.024	0.010	1.426	0.202	0.255
AB-45-1	80.38	0.98	0.011	7.78	0.85	0.032	0.009	0.018	1.081	0.164	0.312
AB-45-2	79.05	0.98	0.020	7.66	0.83	0.045	0.011	0.014	1.457	0.189	0.241
AB-45-3	80.34	0.96	0.028	7.83	0.69	0.057	0.011	0.022	1.684	0.249	0.308
AB-45-5	84.96	0.96	0.027	8.20	0.87	0.045	0.007	0.060	1.623	0.200	0.253
AB-45-6	82.52	0.97	0.013	7.94	0.91	0.035	0.004	0.020	1.268	0.155	0.214
AB-45-7	81.73	0.95	0.021	7.94	0.69	0.039	0.007	0.019	1.080	0.167	0.208
AB-45-8	81.60	0.94	0.034	7.81	0.86	0.051	0.007	0.013	1.749	0.237	0.321
AB-90-1	75.35	0.94	0.024	7.40	0.68	0.044	0.008	0.013	1.633	0.171	0.325
AB-90-2	78.83	0.91	0.046	7.64	0.81	0.061	0.007	0.027	1.722	0.241	0.427
AB-90-3	76.17	0.91	0.045	7.44	0.51	0.058	0.008	0.015	1.535	0.192	0.253
AB-90-4	77.46	0.89	0.039	7.55	0.74	0.054	0.012	0.018	1.722	0.222	0.296
AB-90-5	78.95	0.91	0.038	7.65	0.86	0.058	0.011	0.019	1.835	0.226	0.432
AB-90-7	77.06	0.94	0.032	7.49	0.83	0.050	0.012	0.020	1.537	0.197	0.254
AB-90-8	75.18	0.94	0.041	7.30	0.77	0.053	0.008	0.019	1.070	0.192	0.239
AB-90-9	79.86	0.95	0.020	7.75	0.88	0.028	0.004	0.040	1.481	0.178	0.230
M-90-2	51.55	0.99	0.002	5.04	0.82	0.012	0.006	0.003	0.919	0.125	0.156
M-90-3	51.77	0.99	0.002	5.04	0.74	0.016	0.009	0.003	0.101	0.007	0.010
M-90-4	51.62	0.99	0.002	5.05	0.79	0.015	0.002	0.006	0.102	0.006	0.008
M-90-5	51.61	0.99	0.002	5.04	0.76	0.015	0.003	0.009	0.122	0.006	0.009
M-90-7	50.16	0.99	0.003	5.02	0.05	0.055	0.006	0.013	0.104	0.007	0.009
M-90-9	50.59	0.99	0.002	4.94	0.90	0.005	0.003	0.003	0.115	0.021	0.065
M-90-10	50.85	0.99	0.002	4.96	0.83	0.012	0.009	0.013	0.082	0.006	0.008

Fig. 7. Setup for axial LCF tests.

2.4. Test setup

The low cycle fatigue behaviour of the WAAM material was examined by means of strain-controlled fatigue testing, undertaken at room temperature in accordance with BS ISO 12106 [36] at the Institute of Metal Research in the Chinese Academy of Science. All coupons were tested under uniaxial cyclic loading and subjected to fully reversed constant total strain amplitude cycles – see Fig. 7. Different total strain amplitudes within the LCF regime were considered, ranging from ± 0.2% to ± 2%. Cyclic loading was applied under displacement control using a 100 kN Instron actuator at a frequency of 0.1 Hz, while a 10 mm (less than the parallel length of 20 mm) extensometer was used to measure the deformations of the coupons. Displacement control was employed for safety reasons, to allow for the onset of cracking beyond

Table 4
Results of low cycle fatigue tests.

Specimen	$\Delta\varepsilon/2$ (%)	$\Delta\varepsilon_e/2$ (%)	$\Delta\varepsilon_p/2$ (%)	$\Delta\sigma/2$ (MPa)	N_f
AB-0-1	0.20	0.1346	0.0654	274.34	2450
AB-0-2	0.20	0.1301	0.0699	265.22	2960
AB-0-3	0.50	0.1462	0.3528	298.02	700
AB-0-4	0.50	0.1494	0.3506	304.43	885
AB-0-5	1.00	0.1612	0.8388	328.48	423
AB-0–6	1.00	0.1684	0.8316	343.11	231
AB-0-8	1.20	0.1785	1.0215	363.79	278
AB-0-9	1.70	0.1873	1.5127	381.67	71
AB-0-10	1.50	0.1739	1.3261	354.50	180
AB-45-1	0.20	0.1247	0.0753	251.72	1700
AB-45-2	1.20	0.1706	1.0294	344.34	93
AB-45-3	0.50	0.1415	0.3585	285.76	371
AB-45-5	0.20	0.1188	0.0812	239.92	1120
AB-45-6	1.00	0.1593	0.8407	321.65	194
AB-45-7	1.00	0.1529	0.8471	308.61	197
AB-45-8	1.20	0.1593	1.0407	321.59	84
AB-90-1	2.00	0.1845	1.8155	367.20	27
AB-90-2	0.20	0.1324	0.0676	263.56	1090
AB-90-3	1.50	0.1824	1.3196	362.93	29
AB-90-4	1.00	0.1620	0.8380	322.31	50
AB-90-5	1.00	0.1738	0.8272	345.86	39
AB-90-7	0.50	0.1427	0.3563	284.06	400
AB-90-8	0.50	0.1470	0.3530	292.49	520
AB-90-9	0.20	0.1257	0.0743	250.12	1450
M-90-2	0.20	0.1324	0.0676	270.69	6720
M-90-3	0.20	0.1423	0.0577	291.07	3130
M-90-4	0.50	0.1606	0.3394	328.49	1000
M-90-5	0.50	0.1596	0.3404	326.36	691
M-90-7	1.00	0.1633	0.8357	333.96	562
M-90-9	1.50	0.1663	1.3337	340.13	330
M-90-10	2.00	0.1736	1.8264	355.10	104

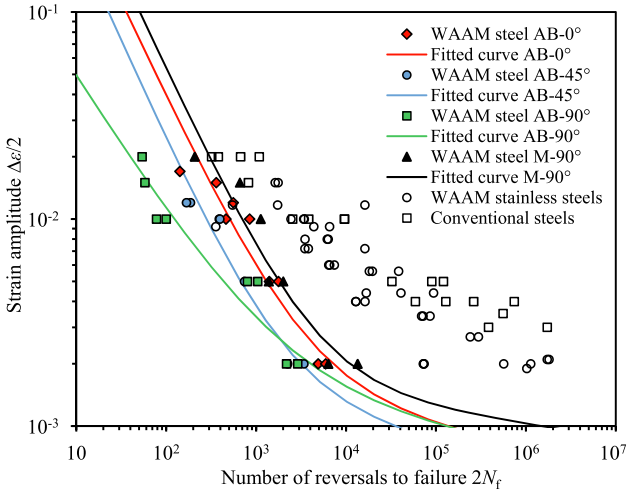

Fig. 8. Strain-life test data and fitted curves for WAAM steel, together with existing data on WAAM stainless steels and conventional structural steels.

Table 5
Parameters of Manson-Coffin-Basquin law and cyclic stress-strain curve.

Surface finish	θ	σ_f'	b	ε_f'	c	K	n
As-built	0°	646.29	−0.102	2.765	−0.932	811.69	0.172
As-built	45°	596.50	−0.111	2.106	−0.98	881.29	0.202
As-built	90°	502.03	−0.084	0.235	−0.693	756.99	0.161
Machined	90°	522.60	−0.066	3.957	−0.941	491.37	0.070

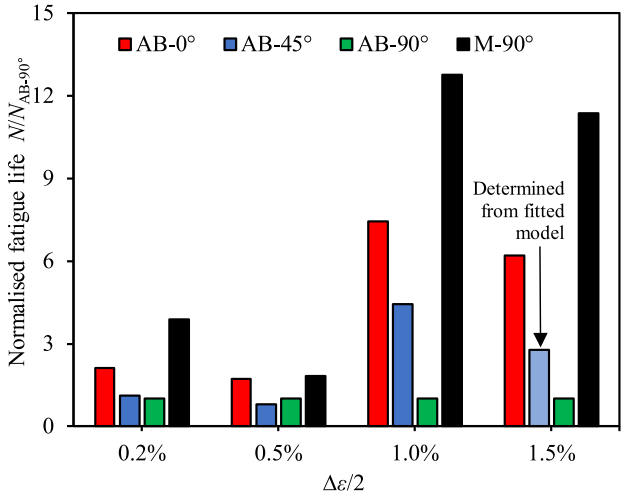

Fig. 9. Comparison of fatigue life among WAAM coupons with different finishes (AB = as-built; M = machined) and loading directions.

the measuring region of the extensometer, since such cracking could not be detected under strain control, leading to the delayed termination of testing. Good precision (±0.005%) was obtained for the strain data under the displacement control loading, as also observed in LCF tests in [37]. During the initial stage of the tests, the amplitudes of the applied displacements were slightly adjusted, according to the readings from the extensometer, to achieve the target strain amplitudes. Upon stabilisation, testing progressed until the occurrence of fracture, and failure was defined at the point of a 20% drop in load.

3. Experimental results and discussion

In this section, the results of the constant strain amplitude fatigue tests are presented and discussed. Strain-life relationships and cyclic stress-strain curves are developed for the WAAM material. The failure mechanisms of the tested coupons are also analysed through fractography.

3.1. Strain-life relationship

The Coffin-Manson equation [38,39], as given by Eq. (4), is widely used to represent the relationship between the plastic strain amplitude $\Delta\varepsilon_p/2$ and fatigue life N_f of metals in the low cycle high strain fatigue regime, while Basquin's equation [40], as given by Eq. (5), describes the high cycle low strain behaviour.

$$\frac{\Delta\varepsilon_p}{2} = \varepsilon_f'(2N_f)^c \tag{4}$$

$$\frac{\Delta\varepsilon_e}{2} = \frac{\Delta\sigma}{2E} = \frac{\sigma_f'}{E}(2N_f)^b \tag{5}$$

where σ_f' is the fatigue strength coefficient, b is the fatigue strength exponent, ε_f' is the fatigue ductility coefficient, c is the fatigue ductility exponent, $2N_f$ is the number of reversals to failure and E is the Young's modulus determined from the tensile tests (see Table 2), as adopted in [41,42]. Combining Eqs (4) and (5) leads to the Manson-Coffin-Basquin equation, as given by Eq. (6), which sums the elastic and plastic strains into a total strain.

$$\frac{\Delta\varepsilon}{2} = \frac{\Delta\varepsilon_e}{2} + \frac{\Delta\varepsilon_p}{2} = \frac{\sigma_f'}{E}(2N_f)^b + \varepsilon_f'(2N_f)^c \tag{6}$$

The Manson-Coffin-Basquin equation is adopted herein to describe the strain-life relationships obtained from the fatigue tests. The results of the low cycle fatigue tests are presented in Table 4. The total strain amplitudes $\Delta\varepsilon/2$ and the stress amplitudes at half of the number of cycles to failure $\Delta\sigma/2$ were measured in the tests. The elastic strain amplitudes $\Delta\varepsilon_e/2$ were calculated using Eq. (5), while the plastic strain amplitudes $\Delta\varepsilon_p/2$ were then obtained from the differences between the total strain amplitudes and the elastic strain amplitudes.

The Manson-Coffin-Basquin equation (Eq. (6)) is fitted to the strain-life data on the θ = 0°, 45° and 90° as-built coupons and θ = 90° machined coupons in double logarithmic coordinates in Fig. 8, and the fitted model coefficients are reported in Table 5. As expected, the strain-life data exhibit the trend of decreasing fatigue life with increasing total strain amplitude. It can be seen that the Manson-Coffin-Basquin equation generally provides good predictions of the low cycle fatigue life of WAAM ER70S-6 steel. The strain-life data on the examined WAAM steel are also compared against existing data on machined WAAM stainless steels [26,43] and conventionally produced structural steels (both with smooth surfaces) [44] in Fig. 8. It can be seen that the studied WAAM steel exhibits inferior low cycle fatigue behaviour compared to WAAM stainless steels and conventional steels, especially under lower strain amplitudes.

The influence of the surface topography on the fatigue performance of WAAM ER70S-6 steel was evaluated by comparing the test results of the machined coupons and the as-built coupons tested in different directions. The average fatigue life of each group of specimens for each strain amplitude N is normalised by the average fatigue life of the θ = 90° as-built coupons $N_{AB\text{-}90°}$ and plotted in Fig. 9. The presented data were predominantly derived from the cyclic test results, except for one data point (missing due to the occurrence of buckling during testing) being back-calculated using the fitted Manson-Coffin-Basquin model – see Fig. 9. For all applied strain amplitudes, the machined coupons exhibited superior low cycle fatigue performance compared to the as-built coupons. Further, the negative influence of the undulating as-

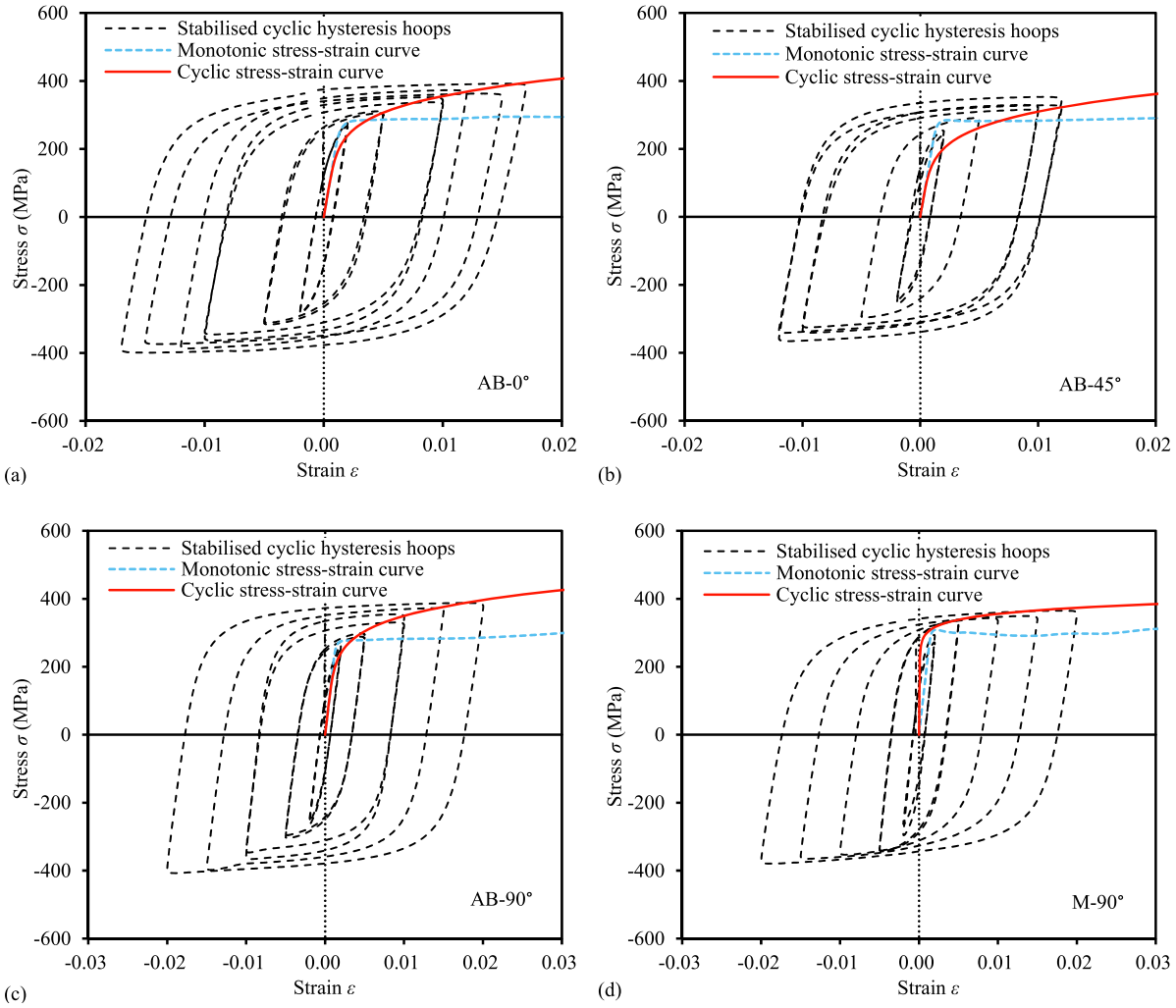

Fig. 10. Monotonic and cyclic stress-strain curves and stabilised hysteresis loops of WAAM ER70S-6 steel: (a) AB-0°; (b) AB-45°; (c) AB-90°; (d) M-90° (AB = as-built; M = machined).

built geometry was most significant for the $\theta = 90°$ coupons for most strain amplitudes (except for ± 0.5%), and generally became more pronounced with increasing strain amplitude, with reductions in fatigue life (i.e. $N_{\text{AB-90°}}$ relative to $N_{\text{M-90°}}$) of about 75% and 90% at ±0.2% and ±1.5% strain amplitudes, respectively. Overall, the normalised fatigue lives ($N/N_{\text{AB-90°}}$) tended to decrease with increasing angle of testing θ, attributed to the increasing geometric variability [13] discussed in Section 2.2.

3.2. Cyclic stress-strain curves

When a family of stabilised hysteresis loops with various strain amplitudes is plotted on the same graph, a cyclic stress-strain curve can be defined by tracing the locus of the tips of the loops [45]. The cyclic stress-strain curve can be represented by a form of Ramberg-Osgood relationship, as given by:

$$\frac{\Delta\varepsilon}{2} = \frac{\Delta\sigma}{2E} + \left(\frac{\Delta\sigma}{2K}\right)^{1/n} \tag{7}$$

where $\Delta\varepsilon/2$ is the total strain amplitude, $\Delta\sigma$ is the stabilised stress amplitude at half of the number of cycles to failure, E is the Young's modulus determined from the tensile tests – see Table 2, K is the cyclic strength coefficient and n is the cyclic strain hardening exponent. The material constants K and n were determined for the studied WAAM steel by fitting a power law to the obtained stress amplitude versus plastic strain amplitude experimental data, as presented in Table 5.

The stabilised cyclic stress-strain hysteresis loops, monotonic stress-strain curves and cyclic stress-strain curves of the examined WAAM material, including the two different surface finishes and three different loading directions, are presented in Fig. 10. The WAAM steel is shown to exhibit strong cyclic hardening in both the machined and as-built conditions and in the different loading directions; as the strain amplitude increases, the stabilised stress amplitude rises substantially to values much higher than the ultimate stress reached in the monotonic tensile tests. The rate and extent of cyclic hardening may also be assessed by examining the progression of stress amplitude at each cycle throughout the tests. This is shown at the different considered strain amplitudes (from ±0.2% to ±2%) in Fig. 11. It can be seen that almost all specimens subjected to medium-to-high strain amplitudes (beyond ±0.5%) exhibited cyclic hardening during the first few cycles, followed by softening alone or softening and re-hardening until fatigue failure, while specimens subjected to lower strain amplitudes (i.e. ±0.2%) underwent

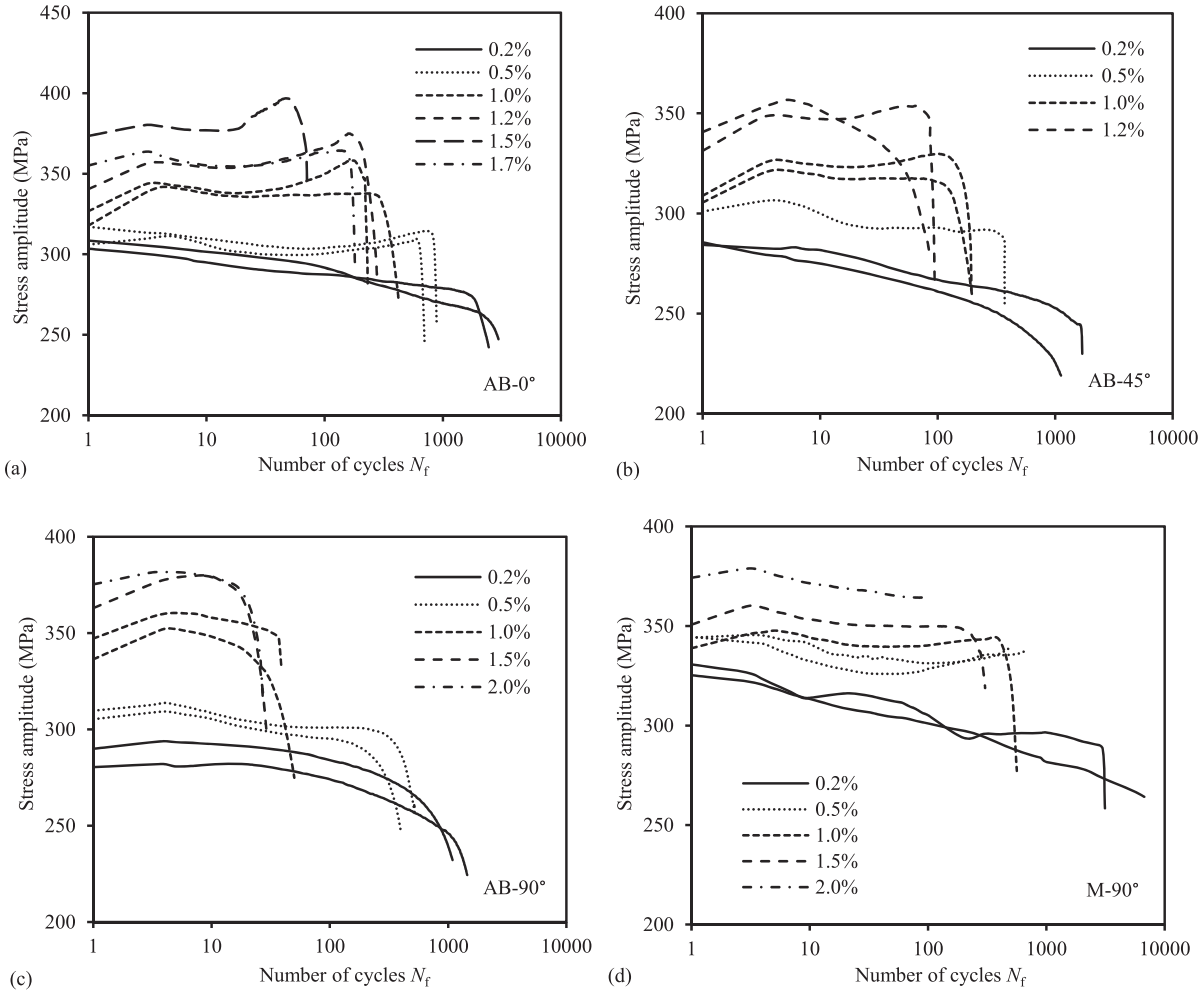

Fig. 11. Variation of stress amplitudes during tests at different strain amplitudes for WAAM ER70S-6 steel: (a) AB-0°; (b) AB-45°; (c) AB-90°; (d) M-90° (AB = as-built; M = machined).

continuous cyclic softening until failure. Similar cyclic hardening and softening behaviour has also been observed in [45,46].

To further examine the cyclic hardening/softening behaviour of the studied WAAM material, the concepts of strain ratio *SR* and hardening factor *H* are introduced as follows[47].

$$SR = \frac{\Delta\varepsilon_p}{\Delta\varepsilon_e} = \frac{\Delta\varepsilon - \Delta\varepsilon_e}{\Delta\varepsilon_e} = \frac{E\Delta\varepsilon}{\Delta\sigma} - 1 \tag{8}$$

$$H = \frac{SR_i}{SR_1} \tag{9}$$

where *SR* represents the ratio of the plastic strain to the elastic strain within each hysteresis curve and *H* is the ratio of the strain ratio at each cycle SR_i and the strain ratio at the first cycle SR_1. It is clear that for cycle-hardening materials, $H < 1$, while for cycle-softening materials, $H > 1$. The variation of the hardening factor with the number of cycles for the WAAM coupons is illustrated in Fig. 12. It can be seen that the studied WAAM ER70S-6 steel generally exhibited cyclic hardening throughout the low cycle fatigue life under most of the imposed strain amplitudes; the exception was the strain amplitude of 0.2%, in the case of which cyclic softening occurred in the later stages of the fatigue loading.

A material is said to exhibit Masing behaviour if the loading (or unloading) branches of the hysteresis loops obtained at different strain amplitudes are the same [48]. The cyclic stress-strain curves of a Masing-type material have similar shapes to the stabilised hysteresis loops, facilitating direct calculations of the plastic hysteresis energy for each cycle and hence the use of energy approaches for fatigue life predictions [49]. In order to investigate the Masing behaviour of WAAM ER70S-6 steel and exclude the influence of the as-built undulating geometry, the cyclic stress-strain behaviour of the machined WAAM material was examined. The stabilised hysteresis loops at the half-life of the machined coupons are plotted in Fig. 13, with the lower vertices of all curves shifted to a common origin. It can be seen that, when the total strain amplitude was less than 0.5%, the material exhibited typical Masing behaviour, with the ascending parts of the hysteresis curves for different strain amplitudes being almost coincident. However, with increasing strain amplitudes, the material displayed non-Masing behaviour, with the upper branches of the hysteresis loops deviating from each other [50]. It has been found that for ferritic-pearlitic steels, Masing behaviour is generally observed under low strain amplitudes, while non-Masing behaviour occurs when the imposed plastic strain exceeds a certain plastic strain range (typically around 0.4%) [51]. This finding also applies to the studied WAAM ER70S-6 steel, which also features a ferritic-pearlitic microstructure, as described in Section 2.2. It can therefore be inferred that the microstructure and dislocation

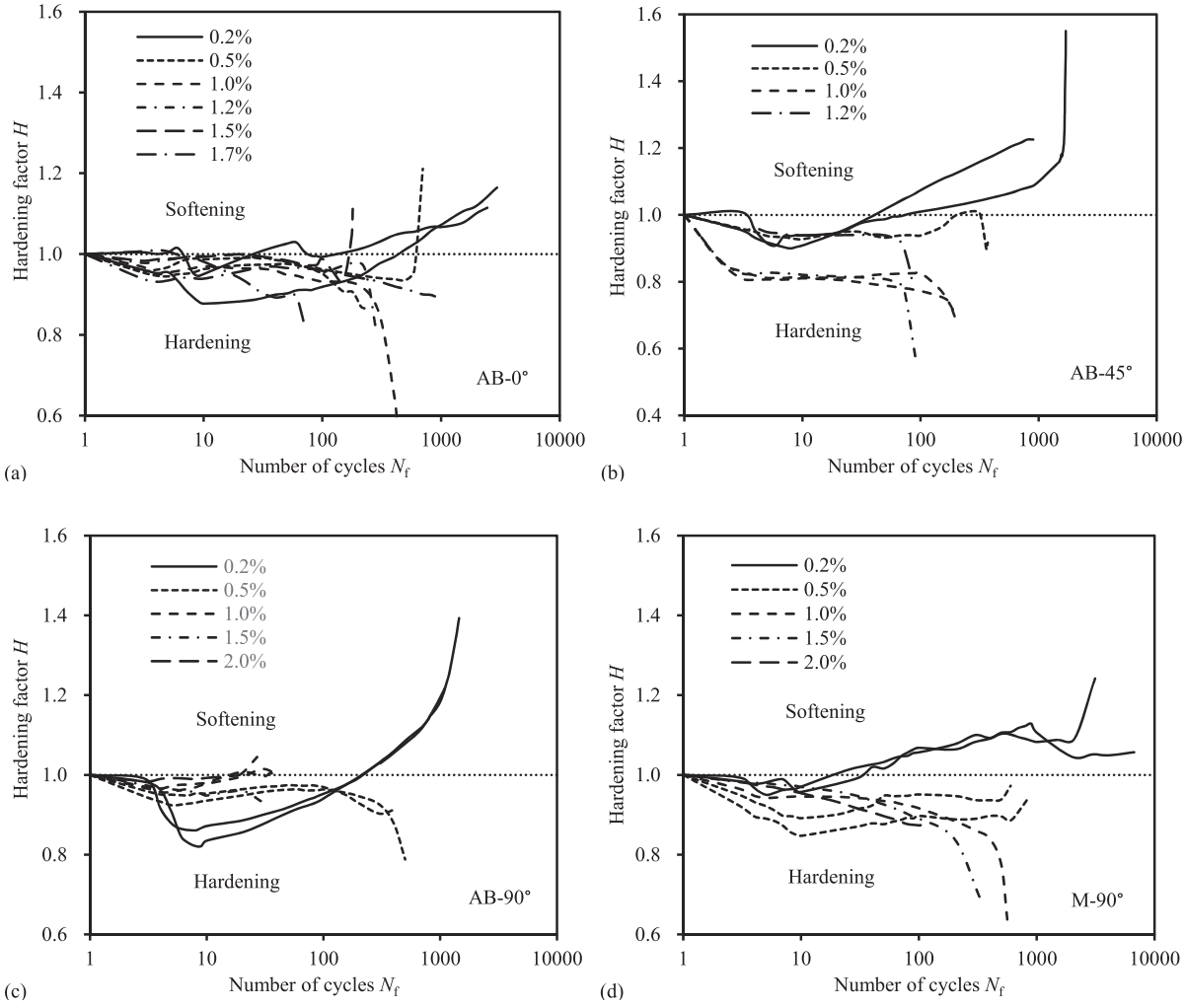

Fig. 12. Variation of hardening factor with the number of cycles for WAAM ER70S-6: (a) AB-0°; (b) AB-45°; (c) AB-90°; (d) M-90° (AB = as-built; M = machined).

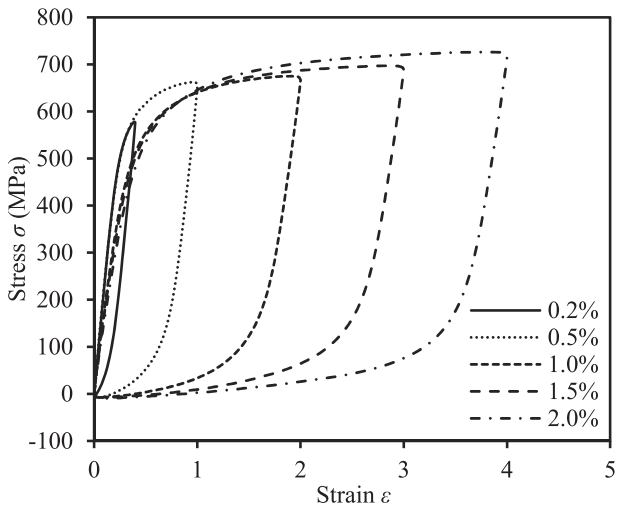

Fig. 13. Half-life hysteresis loops of machined WAAM ER70S-6 steel with lower tips shifted to a common origin.

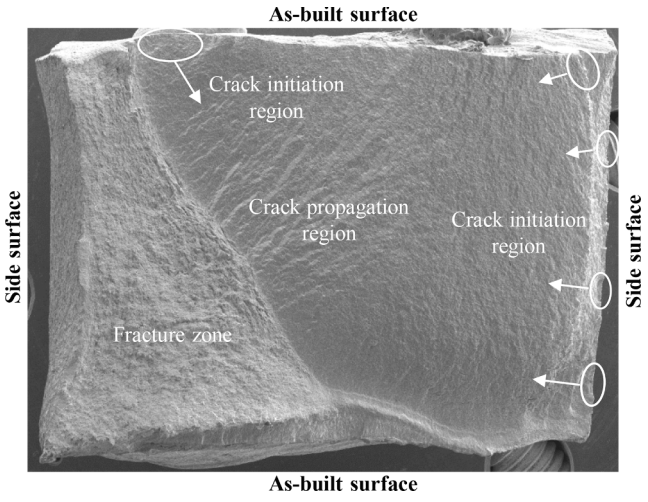

Fig. 14. Fracture surface of Coupon AB-90-2.

substructure of the studied WAAM ER70S-6 steel were not stable when subjected to large cyclic strains [48], leading to the significant non-Masing behaviour. Note that under the ±0.2% and ±0.5% strain amplitude cyclic loading, the initial elastic modulus values of the coupons were almost equal to those determined from the monotonic tensile

tests, though with a 10%-20% reduction before fracture. However, under the larger strain amplitudes (i.e. ±1.0%, ±1.5% and ±2.0%), the initial cyclic elastic modulus values were about 10% lower than their monotonic counterparts, followed by further reductions shortly before failure.

3.3. Fractographic analysis

Fractography was carried out on the tested WAAM coupons using scanning electron microscopy (SEM), in order to examine their failure mechanisms under low cycle fatigue loading. A typical fracture surface of a tested WAAM coupon is shown in Fig. 14, which demonstrates three major regions: the crack initiation region, the crack propagation region and the fracture zone, with the latter featuring a rougher surface. Micro-cracks initiated at different locations on the fracture surface, developing into an irregular (rather than the common arc) shape – see Fig. 14. It can be seen that fracture of the coupon occurred following a major crack initiating from the as-built surface and propagating inwards, as well as to multiple minor cracks initiating and growing from the side surface. The fatigue crack propagation zone and fracture zone can be clearly identified from the fracture surface of the coupon, while the boundary between the crack initiation and propagation stages is indiscernible. For the studied low cycle fatigue coupons, the crack initiation stage represents most of the fatigue life, while the crack propagation stage represents only a fraction. Further investigation is nonetheless needed for explicit distinctions to be made between the two stages.

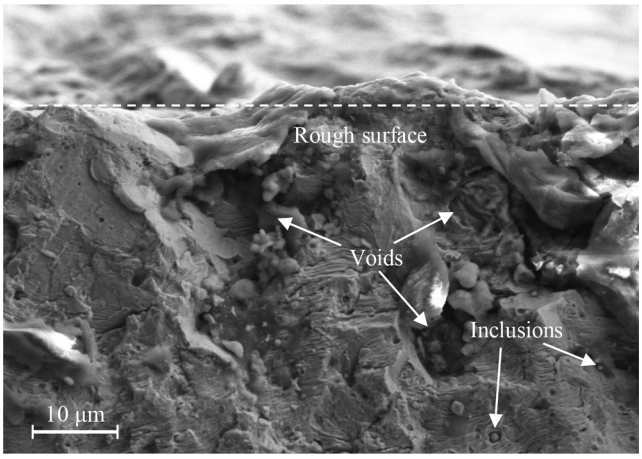

Fig. 15. Crack initiation region of Coupon AB-90-8.

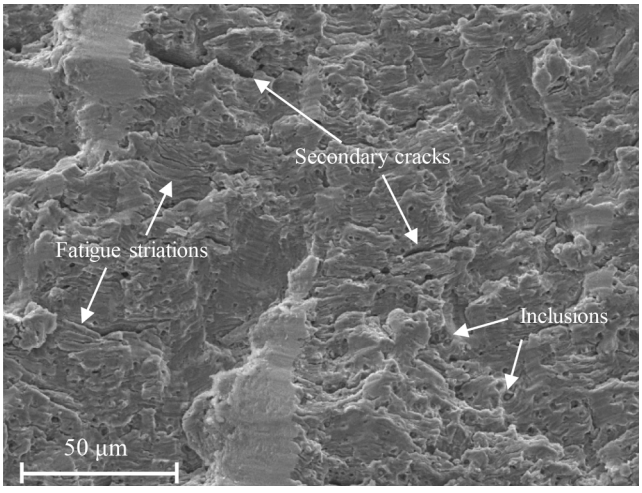

Fig. 16. Crack propagation region of Coupon AB-90-2.

The irregular profiles of the as-built WAAM coupons and the voids and inclusions [52] within the material, as illustrated in Fig. 15, would have triggered local stress concentrations in the coupons, accelerating the initiation of fatigue cracks and hence the occurrence of fracture. The presence of voids and inclusions within the WAAM material would have influenced both the crack initiation and the crack propagation stages. The micromorphology of a typical portion of the fatigue crack propagation zone is shown in Fig. 16, where fatigue striations, secondary cracks and inclusions can be observed.

A wide range of strain amplitudes were covered in the low cycle fatigue tests, resulting in the tested WAAM coupons having different failure mechanisms. Under medium to high strain amplitudes, the WAAM material generally exhibited ductile fracture characteristics, reflected by the presence of a large number of regular dimples (approximately 2 μm in size) in the fracture zone. However, for the coupons tested under low strain amplitudes, in addition to the dimples in the fracture zone, a more brittle cleavage failure was observed – see Fig. 17.

Multiple crack initiation sites were not only observed in the fracture surfaces (see Fig. 14), but also at different locations along the length direction of the as-built coupons, as shown in Fig. 18 owing to their undulating geometries. For the $\theta = 45^{\circ}$ coupons, fatigue cracks often initiated at the geometric discontinuities at the coupons edges and extended diagonally along the print layers. Overall, the low cycle fatigue performance of the WAAM material was clearly adversely influenced by local stress concentrations induced by microscopic defects and the as-built geometric undulations.

4. Conclusions

An experimental study into the low cycle fatigue (LCF) behaviour of WAAM ER70S-6 steel has been presented. A total of 31 as-built and machined coupons have been tested at three different directions relative to the print layer orientation (0°, 45° and 90°) under constant amplitude LCF loading, covering a range of strain amplitudes from ±0.2% to ±2.0%. Strain-life relationships and cyclic stress-strain curves were derived from the obtained experimental data. In parallel with the LCF testing, fractography was also conducted to examine the failure mechanisms of the WAAM coupons.

The machined WAAM steel exhibited marginally inferior LCF performance to conventionally-produced steels, attributed to the greater prevalence of microscopic defects (e.g. voids and inclusions). The material also exhibited significant non-Masing behaviour. The geometric undulations of the as-built coupons led to a degree of anisotropy and further reductions in the LCF properties, owing to the increased susceptibility to local stress concentrations. The cyclic hardening/softening responses and failure mechanisms of the WAAM coupons were related to the imposed strain amplitudes. Higher strain amplitudes generally led to cyclic hardening and ductile fracture, while cyclic softening and more brittle fatigue failure was seen at lower strain amplitudes.

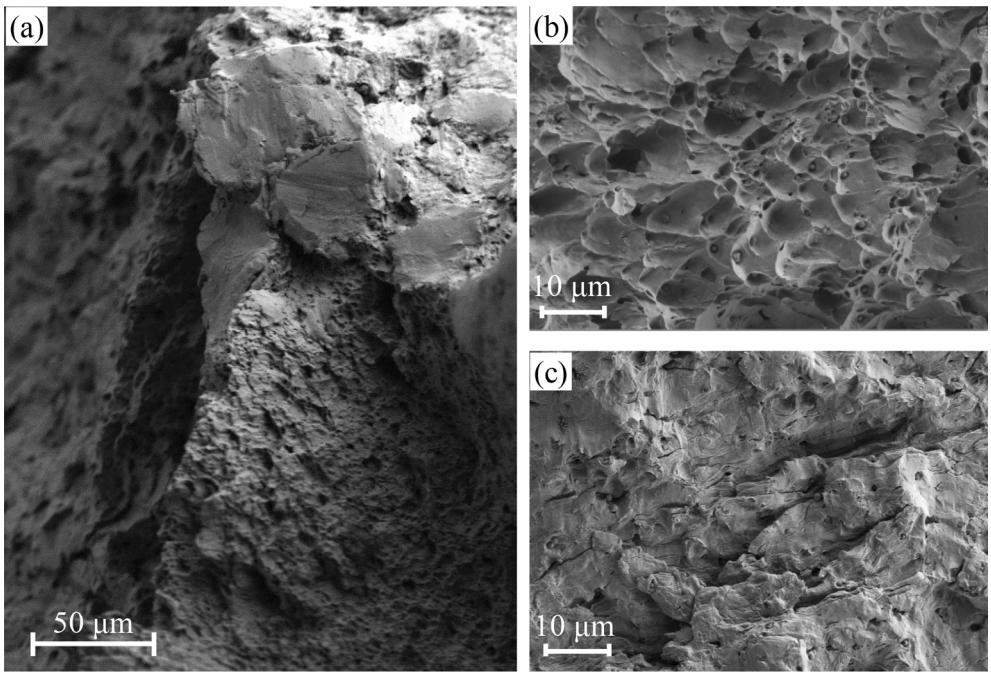

Fig. 17. Fracture zone of Coupon AB-90-8: (a) edge; (b) dimples; (c) cleavage failure.

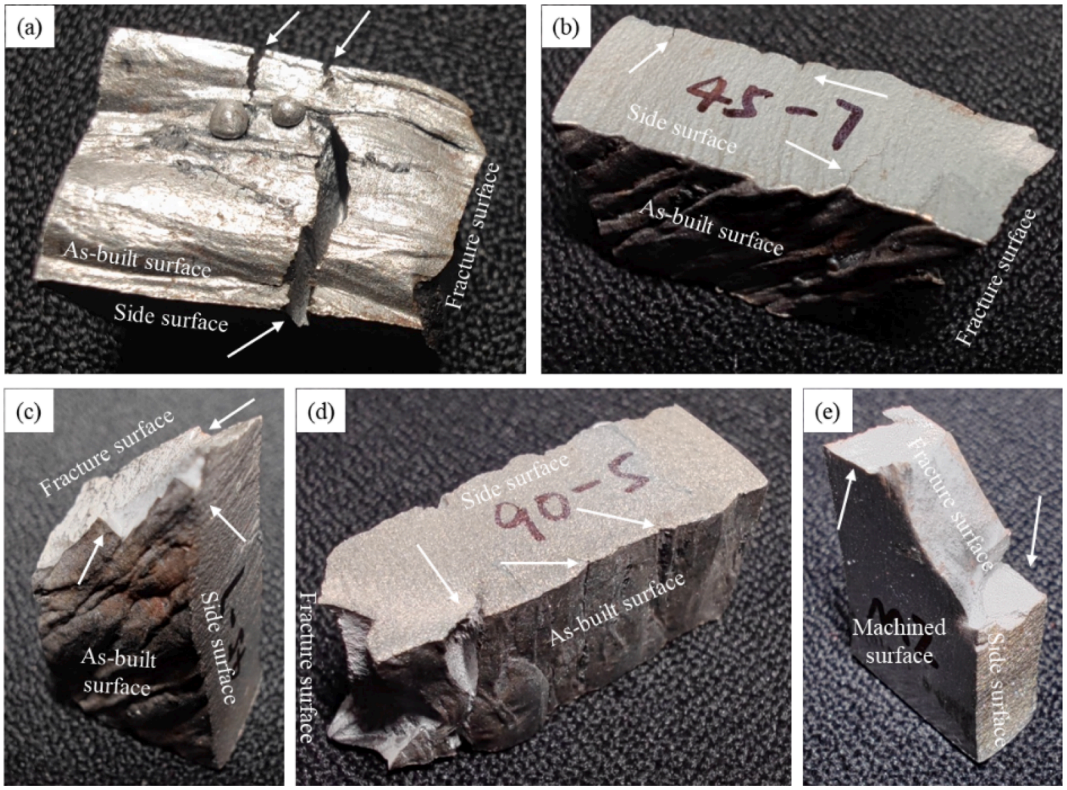

Fig. 18. Multi-source fatigue cracking of WAAM ER70S-6: (a) AB-0° (b-c) AB-45° (d) AB-90° (e) M-90°.

CRediT authorship contribution statement

Liang Zong: Conceptualization, Investigation, Methodology, Project administration, Resources, Supervision, Writing – review & editing. **Wanquan Fang:** Formal analysis, Investigation, Methodology, Software, Visualization, Writing – original draft, Writing – review & editing. **Cheng Huang:** Formal analysis, Investigation, Methodology, Software, Visualization, Writing – original draft, Writing – review & editing. **Zhongxing Wang:** Conceptualization. **Leroy Gardner:** Conceptualization, Funding acquisition, Investigation, Methodology, Project administration, Resources, Supervision, Writing – review & editing.

Declaration of Competing Interest

The authors declare that they have no known competing financial interests or personal relationships that could have appeared to influence the work reported in this paper.

Data availability

Data will be made available on request.

Acknowledgements

This research was possible thanks to funding and support from the European Union's Horizon 2020 research and innovation programme under grant agreement No. 820776 'Intelligent data driven pipeline for the manufacturing of certified metal parts through Direct Energy Deposition process (INTEGRADDE).' The authors also gratefully acknowledge MX3D for the provision of the test specimens.

References

[1] Gardner L. Metal additive manufacturing in structural engineering – review, advances, opportunities and outlook. Structures 2023;47:2178–93.
[2] Kühne R, Feldmann M, Citarelli S, Reisgen U, Sharma R, Oster L. 3D printing in steel construction with the automated Wire Arc Additive Manufacturing. ce/papers 2019;3(3–4):577–83.
[3] Syuhada A, Shamsudin M S, Omar M F, Ghoshal S K, Harun S W, Aziz M S. Incorporating 3D metal printing with artificial intelligence in meeting aerospace demands. Journal of Physics: Conference Series. IOP Publishing, 2021; 1892(1): 012015.
[4] Romero PE, Arribas-Barrios J, Rodriguez-Alabanda O, González-Merino R, Guerrero-Vaca G. Manufacture of polyurethane foam parts for automotive industry using FDM 3D printed molds. CIRP J Manuf Sci Technol 2021;32:396–404.
[5] Mishra A, Srivastava V. Biomaterials and 3D printing techniques used in the medical field. J Med Eng Technol 2021;45(4):290–302.
[6] Kanyilmaz A, Demir AG, Chierici M, Berto F, Gardner L, Kandukuri SY, et al. Role of metal 3D printing to increase quality and resource-efficiency in the construction sector. Addit Manuf 2022;50:102541.
[7] Shah IH, Hadjipantelis N, Walter L, Myers RJ, Gardner L. Environmental life cycle assessment of wire arc additively manufactured structural components. J Clean Prod 2023;389:136071.
[8] Feucht T, Lange J, Erven M. 3D-printing with steel: Additive manufacturing of connection elements and beam reinforcements. ce/papers 2019;3(3–4):343–8.
[9] Laghi V, Palermo M, Gasparini G, Trombetti T. Computational design and manufacturing of a half-scaled 3D-printed stainless steel diagrid column. Addit Manuf 2020;36:101505.
[10] Lange J, Feucht T, Erven M. 3D-printing with steel-additive manufacturing connections and structures. ce/papers 2021;4(2–4):2–7.
[11] Gardner L, Kyvelou P, Herbert G, Buchanan C. Testing and initial verification of the world's first metal 3D printed bridge. J Constr Steel Res 2020;172:106233.
[12] Kyvelou P, Buchanan C, Gardner L. Numerical simulation and evaluation of the world's first metal additively manufactured bridge. Structures 2022;42:405–16.
[13] Huang C, Kyvelou P, Zhang R, Britton TB, Gardner L. Mechanical testing and microstructural analysis of wire arc additively manufactured steels. Mater Des 2022;216:110544.
[14] Kyvelou P, Slack H, Mountanou DD, Wadee M, Britton T, Buchanan C, et al. Mechanical and microstructural testing of wire and arc additively manufactured sheet material. Mater Des 2020;192:108675.
[15] Laghi V, Palermo M, Gasparini G, Girelli VA, Trombetti T. On the influence of the geometrical irregularities in the mechanical response of Wire-and-Arc Additively Manufactured planar elements. J Constr Steel Res 2021;178:106490.
[16] Kyvelou P, Huang C, Gardner L, Buchanan C. Structural testing and design of wire arc additively manufactured square hollow sections. J Struct Eng 2021;147(12): 04021218.
[17] Huang C, Meng X, Gardner L. Cross-sectional behaviour of wire arc additively manufactured tubular beams. Eng Struct 2022;272:114922.
[18] Meng X, Weber B, Nitawaki M, Gardner L. Optimisation and testing of wire arc additively manufactured steel stub columns. Thin-Walled Struct 2023;189:110857.
[19] Huang C, Meng X, Buchanan C, Gardner L. Flexural buckling of wire arc additively manufactured tubular columns. J Struct Eng 2022;148(9):04022139.
[20] Weber B, Meng X, Zhang R, Nitawaki M, Sagawa T, Gardner L. Tensile behaviour of WAAM high strength steel material and members. Mater Des. (submitted).
[21] Guo X, Kyvelou P, Ye J, Teh LH, Gardner L. Experimental investigation of wire arc additively manufactured steel single-lap shear bolted connections. Thin-Walled Struct 2022;181:110029.
[22] Guo X, Kyvelou P, Ye J, The LH, Gardner L. Experimental study of DED-arc additively manufactured steel double-lap shear bolted connections. Eng Struct 2023;281:115736.
[23] Guo X, Kyvelou P, Ye J, Gardner L. Experimental investigation of wire arc additively manufactured steel T-stub connections. J Constr Steel Res 2023;211: 108106.
[24] Ye J, Kyvelou P, Gilardi F, Lu H, Gilbert M, Gardner L. An end-to-end framework for the additive manufacture of optimized tubular structures. IEEE Access 2021;9: 165476–89.
[25] Xin H, Correia JAFO, Veljkovic M, Zhang Y, Berto F, de Jesus AMP. Probabilistic strain-fatigue life performance based on stochastic analysis of structural and WAAM-stainless steels. Eng Fail Anal 2021;127:105495.
[26] Li Y, Yuan Y, Wang D, Fu S, Song D, Vedani M, et al. Low cycle fatigue behaviour of wire arc additive manufactured and solution annealed 308L stainless steel. Addit Manuf 2022;52:102688.
[27] Samadian K, De Waele W. Fatigue crack growth model incorporating surface waviness for wire+arc additively manufactured components. Procedia Struct Integrity 2020;28:1846–55.
[28] Bartsch H, Kühne R, Citarelli S, Schaffrath S, Feldmann M. Fatigue analysis of wire arc additive manufactured (3D printed) components with unmilled surface. Structures 2021;31:576–89.
[29] Bercelli L, Doudard C, Calloch S, Le Saux V, Beaudet J. Thermometric investigations for the characterization of fatigue crack initiation and propagation in Wire and Arc Additively Manufactured parts with as-built surfaces. Fatigue Fract Eng Mater Struct 2023;46(1):153–70.
[30] Ermakova A, Mehmanparast A, Ganguly S, Razavi J, Berto F. Investigation of mechanical and fracture properties of wire and arc additively manufactured low carbon steel components. Theor Appl Fract Mech 2020;109:102685.
[31] He J, Feng X, Wang X, Guan X. Fatigue performance and acoustic emission behavior of remanufactured low-carbon steel made by wire and arc additive manufacturing. Int J Fatigue 2022;165:107190.
[32] Huang C, Zheng Y, Chen T, Ghafoori E, Gardner L. Fatigue crack growth behaviour of wire arc additively manufactured steels. Int J Fatigue 2023;173:107705.
[33] Huang C, Li L, Pichler N, Ghafoori E, Susmel L, Gardner L. Fatigue testing and analysis of steel plates manufactured by wire-based directed energy deposition. Addit Manuf 2023;73:103696.
[34] MX3D Webpage, www.mx3d.com 2022.
[35] Huang C, Kyvelou P, Gardner L. Stress-strain curves for wire arc additively manufactured steels. Eng Struct 2023;279:115628.
[36] ISO 12106: 2017. Metallic Materials-Fatigue Testing-Axial-Strain-Controlled Method. British Standard, BSI Standards Publication; 2017.
[37] Htoo AT, Miyashita Y, Otsuka Y, Mutoh Y, Sakurai S. Notch fatigue behavior of Ti-6Al-4V alloy in transition region between low and high cycle fatigue. Int J Fatigue 2017;95:194–203.
[38] Coffin Jr LF. A study of the effects of cyclic thermal stresses on a ductile metal. Transactions of the American Society of Mechanical Engineers, New York 1954;76 (6):931–49.
[39] Manson SS. Behavior of materials under conditions of thermal stress. National Advisory Committee for Aeronautics; 1953.
[40] Basquin OH. The exponential law of endurance tests. Proc Am Soc Test Mater 1910; 10:625–30.
[41] Ricotta M. Simple expressions to estimate the Manson-Coffin curves of ductile cast irons. Int J Fatigue 2015;78:38–45.
[42] Niesłony A, el Dsoki C, Kaufmann H, Krug P. New method for evaluation of the Manson–Coffin–Basquin and Ramberg-Osgood equations with respect to compatibility. Int J Fatigue 2008;30(10–11):1967–77.
[43] Galan AJ. Fatigue behaviour and mechanical characterization of austenitic stainless-steel components produced through Wire+Arc Additive Manufacturing. Delft University of Technology; 2020. PhD thesis.
[44] de Jesus AMP, Matos R, Fontoura BFC, Rebelo C, Silva LSD, Veljkovic M. A comparison of the fatigue behaviour between S355 and S690 steel grades. J Constr Steel Res 2012;79:140–50.
[45] Nip KH, Gardner L, Davies CM, Elghazouli AY. Extremely low cycle fatigue tests on structural carbon steel and stainless steel. J Constr Steel Res 2010;66(1):96–110.
[46] Cui S, Wang R, You X, Liu Y, Wang Q. On the low cycle fatigue behaviour and fatigue life prediction of Q345 steel. J Exp Mech 2014;5:537–42. in Chinese.
[47] Paul SK, Sivaprasad S, Dhar S, Tarafder S. Cyclic plastic deformation and cyclic hardening/softening behaviour in 304LN stainless steel. Theor Appl Fract Mech 2010;54(1):63–70.
[48] Sivaprasad S, Paul SK, Das A, Narasaiah N, Tarafder S. Cyclic plastic behaviour of primary heat transport piping materials: Influence of loading schemes on hysteresis loop. Mater Sci Eng A 2010;527(26):6858–69.
[49] Liao X, Wang Y, Feng L, Ban H, Chen Y. Fatigue crack initiation and energy-based life analysis for Q345qD bridge steel at low temperatures. J Constr Steel Res 2021; 180:106571.
[50] Branco R, Costa JDM, Berto F, Razavi SMJ, Ferreira JAM, Capela C, et al. Low-cycle fatigue behaviour of AISI 18Ni300 maraging steel produced by selective laser melting. Metals 2018;8(1):32.
[51] Plumtree A, Abdel-Raouf HA. Cyclic stress–strain response and substructure. Int J Fatigue 2001;23(9):799–805.
[52] Hu D, Wang T, Ma Q, Liu X, Shang L, Li D, et al. Effect of inclusions on low cycle fatigue lifetime in a powder metallurgy nickel-based superalloy FGH96. Int J Fatigue 2019;118:237–48.